








Quasi-periodic Fast Propagating Magnetoacoustic Waves during the Magnetic Reconnection Between Solar Coronal Loops

Leping Li^{1,2,3} , Jun Zhang^{1,3}, Hardi Peter⁴, Lakshmi Pradeep Chitta⁴ , Jiangtao Su^{1,3},
Hongqiang Song² , Chun Xia^{5,6} , and Yijun Hou^{1,3} 

¹ CAS Key Laboratory of Solar Activity, National Astronomical Observatories, Chinese Academy of Sciences, Beijing 100101, People's Republic of China
lepingli@nao.cas.cn

² Shandong Provincial Key Laboratory of Optical Astronomy and Solar-Terrestrial Environment, and Institute of Space Sciences, Shandong University, Weihai, Shandong 264209, People's Republic of China

³ University of Chinese Academy of Sciences, Beijing 100049, People's Republic of China

⁴ Max-Planck Institute for Solar System Research, D-37077 Göttingen, Germany

⁵ School of Physics and Astronomy, Yunnan University, Kunming 650050, People's Republic of China

⁶ Centre for mathematical Plasma Astrophysics, Department of Mathematics, KU Leuven, Celestijnenelaan 200B, B-3001 Leuven, Belgium
Received 2018 September 26; revised 2018 November 12; accepted 2018 November 15; published 2018 November 28

Abstract

Employing *Solar Dynamics Observatory*/Atmospheric Imaging Assembly (AIA) multi-wavelength images, we have presented coronal condensations caused by magnetic reconnection between a system of open and closed solar coronal loops. In this Letter, we report the quasi-periodic fast magnetoacoustic waves propagating away from the reconnection region upward across the higher-lying open loops during the reconnection process. On 2012 January 19, reconnection between the higher-lying open loops and lower-lying closed loops took place, and two sets of newly reconnected loops formed. Thereafter, cooling and condensations of coronal plasma occurred in the magnetic dip region of higher-lying open loops. During the reconnection process, disturbances originating from the reconnection region propagate upward across the magnetic dip region of higher-lying loops with the mean speed and mean speed amplitude of 200 and 30 km s⁻¹, respectively. The mean speed of the propagating disturbances decreases from ~230 km s⁻¹ to ~150 km s⁻¹ during the coronal condensation process, and then increases to ~220 km s⁻¹. This temporal evolution of the mean speed anti-correlates with the light curves of the AIA 131 and 304 Å channels that show the cooling and condensation process of coronal plasma. Furthermore, the propagating disturbances appear quasi-periodically with a peak period of 4 minutes. Our results suggest that the disturbances represent the quasi-periodic fast propagating magnetoacoustic (QFPM) waves originating from the magnetic reconnection between coronal loops.

Key words: magnetic reconnection – plasmas – Sun: corona – Sun: UV radiation – waves

Supporting material: animations

1. Introduction

Magnetic reconnection plays an elemental role in magnetized plasma systems, e.g., solar corona and planetary magnetospheres, throughout the universe (Yamada et al. 2010). It shows the re-configuration of magnetic field geometry, and is used to explain the release of magnetic energy and its conversion to other forms, e.g., thermal, kinetic, and acceleration of nonthermal particles (Aschwanden 2002). The reconnection process is difficult to observe directly. However, because the magnetic flux is frozen into plasma in the solar corona, the coronal structures, e.g., coronal loops, and their evolution usually outline the magnetic field geometry and its change. Remote sensing data has provided a large body of observational evidence of reconnection presented in solar physics, such as X-type structures (Su et al. 2013; Li et al. 2016b), reconnection inflows (Yokoyama et al. 2001; Huang et al. 2018), and outflows (Takasao et al. 2012; Reeves et al. 2015; Li et al. 2016a; Ning 2016), current sheets (Lin et al. 2005; Li et al. 2016c; Xue et al. 2018), plasmoid ejections (Liu et al. 2010; Tian et al. 2014; Cheng et al. 2018), loop-top hard X-ray sources (Masuda et al. 1994; Li & Zhang 2009), cusp-shaped post-flare loops (Tsuneta et al. 1992; Yan et al. 2018), and supra-arcade downflows (McKenzie 2000; Savage & McKenzie 2011).

Numerous theoretical studies of reconnection have been undertaken to explain solar flares (Shibata 1999; Priest & Forbes 2000) that rapidly release the magnetic energy. During the flares, observations of quasi-periodic fast propagating

magnetoacoustic (QFPM) waves have been reported (Liu et al. 2012; Shen et al. 2013; Nisticò et al. 2014). Using Atmospheric Imaging Assembly (AIA; Lemen et al. 2012) images on board the *Solar Dynamics Observatory* (SDO; Pesnell et al. 2012), Liu et al. (2011) presented the QFPM wave trains emanating near a flare kernel, and found the strongest signal with the 181 s period temporally coincides with the flare quasi-periodic pulsations. In another flare, Shen & Liu (2012) noted that almost all of the flare main frequencies are consistent with those of the QFPM waves. QFPM wave trains associated with flaring radio emissions have also been reported (Yuan et al. 2013; Kumar et al. 2017). All of these results suggest the QFPM waves and flares are possibly excited by a common physical origin, i.e., the reconnection periodically releasing magnetic energy (Liu et al. 2011; Shen & Liu 2012; Kumar et al. 2017). However, no reconnection process is observed during these flares. On the other hand, QFPM waves driven by reconnection have been theoretically predicted and simulated (Ofman et al. 2011; Jelínek et al. 2012; Takasao & Shibata 2016). Nevertheless, QFPM waves associated with reconnection directly are rarely observed.

Using AIA multi-wavelength images taken on 2012 January 19, Li et al. (2018) reported the reconnection between two sets of loops and the cooling and condensation of coronal plasma in the magnetic dip (MD) of higher-lying open loops. In this Letter, we reveal the presence of QFPM waves, originating

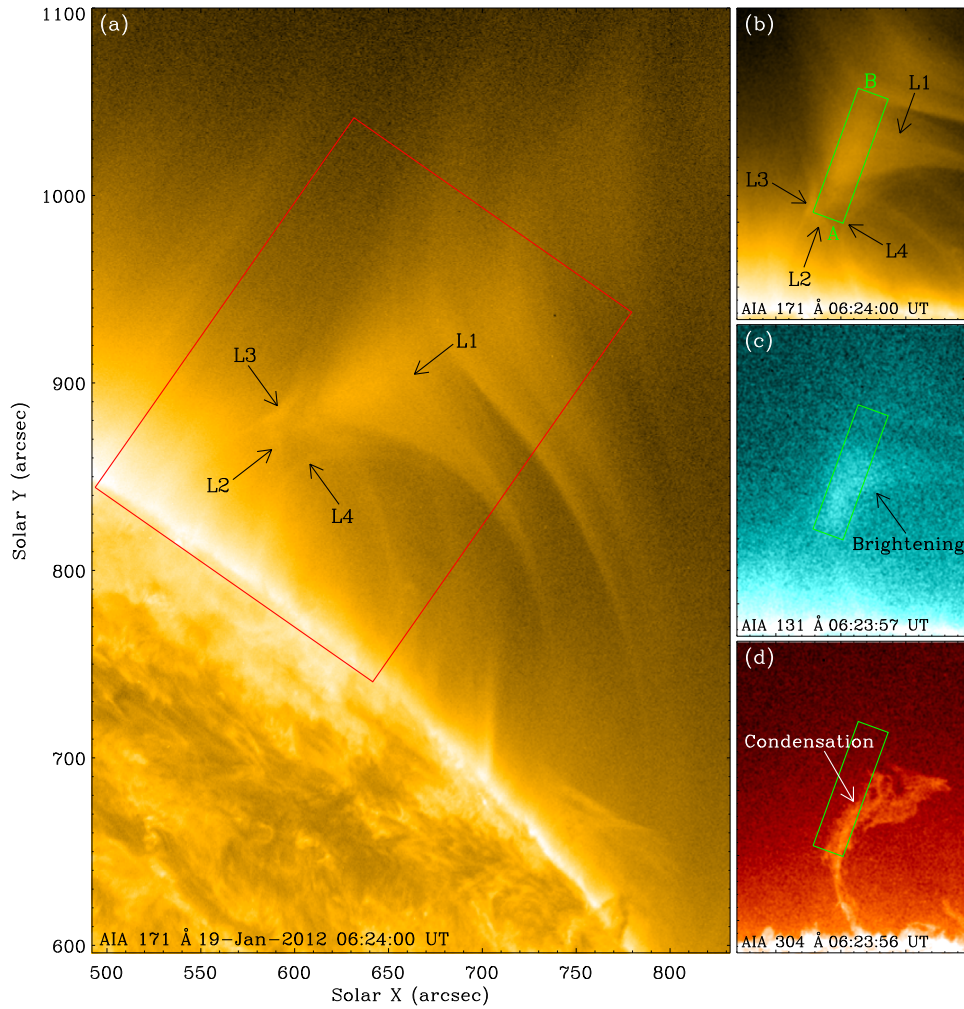


Figure 1. Reconnection between coronal loops and condensations of coronal plasma. AIA 171 (a)–(b), 131 (c), and 304 Å (d) images. The red rectangle in (a) represents the field of view (FOV) of (b)–(d). The green rectangle AB in (b) indicates the position of the time slice of AIA 171 Å images showed in Figure 3(a). The green rectangles in (b)–(d) mark the regions for the light curves of the AIA 171, 131, and 304 Å channels displayed in Figure 4 separately by red, green, and blue lines, respectively. An animation of the three channels is available. It covers 8 hr starting at 01:00 UT in 2012 January 19 and the video duration is 20 s. (An animation of this figure is available.)

from the reconnection region and propagating across the higher-lying loops upward. The observations and results are described in Sections 2 and 3, respectively, and a summary and discussion is given in Section 4.

2. Observations

SDO/AIA is a set of normal-incidence imaging telescopes that obtain images of the solar atmosphere at 10 wavelength channels. Different AIA channels show plasma with different characteristic temperatures, e.g., 304 Å peaks at ~ 0.05 MK (He II), 131 Å peaks at ~ 0.6 MK (Fe VIII) and ~ 10 MK (Fe XXI), and 171 Å peaks at ~ 0.9 MK (Fe IX). In this Letter, AIA 171, 131, and 304 Å images, with spatial sampling and time cadence of $0''.6 \text{ pixel}^{-1}$ and 12 s, are employed to study the QFPM waves and the coronal condensations during the reconnection process.

3. Results

On 2012 January 19, a set of open curved loops, L1, located above the northwestern solar limb, were observed in AIA 171 Å images, see Figure 1(a). From $\sim 01:00$ UT, the loops L1

moved toward the southeast, and reconnected with the lower-lying closed loops, L2. Two sets of newly reconnected loops, L3 and L4, formed and retracted away from the reconnection region. Due to the downward motion, an MD of loops L1 forms. Cooling and condensation of coronal plasma in the MD then takes place. The reconnection site moved to the southwest with a displacement of ~ 35 Mm after $\sim 09:00$ UT; therefore, the reconnection process from 01:00 to 09:00 UT in the region enclosed by a red rectangle in Figure 1(a) is chosen and investigated in detail. To better display evolution of the reconnection, the AIA images are rotated counter-clockwise by an angle of 35° . The portion of the limb in the region of interest, i.e., the red rectangle in Figure 1(a), is thus roughly horizontal in the AIA images presented here, see Figure 1(b). AIA 131 and 304 Å images are illustrated in Figures 1(c)–(d) to show the cooling and condensations of coronal plasma in the MD of loops L1 during the reconnection (see the online animated version of Figures 1(b)–(d)).

During the reconnection process, disturbances are generated from the reconnection region. Figures 2(a)–(b) show the filtered and running difference AIA 171 Å images illustrating the disturbances (see the online animated version of Figure 2).

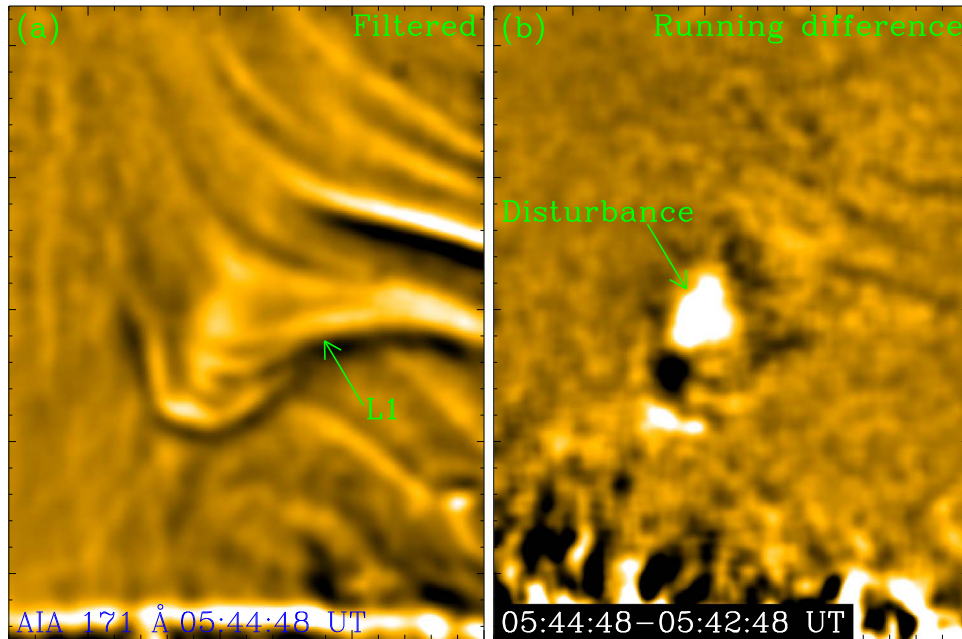


Figure 2. Disturbances propagating from the reconnection region upward across the higher-lying loops. AIA 171 Å filtered (a) and running difference (b) images, with the same FOV as in Figures 1(b)–(d). An animation is available. It covers 5 hr starting at 03:30 UT and the video duration is 63 s. (An animation of this figure is available.)

After the appearance, the disturbances propagate away from the reconnection region and upward across the higher-lying loops. Along the propagating direction AB in the green rectangle in Figure 1(b), a time slice of AIA 171 Å images is made and displayed in Figure 3(a). The green dotted line outlines the downward motion of loops L1, with speeds of 2–9 km s⁻¹. The steep, recurrent stripes show the propagating disturbances across the loops L1. The stripe, marked by red plus symbols, is chosen to display measurements of the beginning time and propagating speed of disturbances. The chosen disturbance appears from ~05:29:12 UT, denoted by the pink triangle in Figure 3(a). The intensities of the AIA 171 Å channel at different positions along the disturbance, marked by the red plus symbols in Figure 3(a), are plotted in Figure 3(b) as black plus symbols. The pink curves in Figure 3(b) show the single Gaussian profiles to the plus symbols. The blue diamonds mark peak positions of the single Gaussian profiles, with 12 s error bars. The red line shows the linear fit to the diamonds, indicating the disturbance propagates at a constant speed of 165 km s⁻¹. Each of the disturbances propagates with a nearly constant speed.

A histogram of the speeds of disturbances is displayed in Figure 3(c). The speeds range from 135 to 265 km s⁻¹ with a mean value of 200 km s⁻¹. Two peaks are identified at 150 and 210 km s⁻¹, respectively. The temporal evolution of the speeds is illustrated in Figure 4 by black plus symbols. The purple diamonds, ranging in 150–230 km s⁻¹ with a mean value of 200 km s⁻¹, represent the mean speeds averaged in 30 minutes. The pink vertical lines denote the speed amplitudes, with a mean value of 30 km s⁻¹ in the range of 15–45 km s⁻¹. The mean speed remains almost constant at ~230 km s⁻¹, then decreases from ~04:00 UT, and reaches the valley of ~150 km s⁻¹ at ~06:00 UT. Thereafter, it increases slowly, and goes back to ~220 km s⁻¹ at ~09:00 UT.

In the propagating path of disturbances, denoted by green rectangles in Figures 1(b)–(d), light curves of the AIA 171,

131, and 304 Å channels are measured and showed in Figure 4 as red, green, and blue curves, respectively. All of the light curves increase first, reach the peaks, and then decrease slowly. However, they peak at different times. The AIA 171 Å light curve peaks at 05:45 UT, but the 131 (304) Å light curve peaks at 06:05 (06:30) UT, 20 (45) minutes later. Because there is no associated bright emission observed in AIA channels showing higher-temperature plasma, e.g., 193, 211, 335, and 94 Å, the enhancement in the AIA 131 Å light curve should originate from cooler (~0.6 MK) plasma rather than from hotter (~10 MK) regions. The AIA 171, 131, and 304 Å light curves thus clearly represent the cooling and condensation process of hotter plasma in the MD of loops L1 (see the online animated version of Figures 1(b)–(d)). The plasma cools down from ~0.9 MK, the characteristic temperature of AIA 171 Å channel, to ~0.6 MK, the characteristic temperature of AIA 131 Å channel, in ~20 minutes, and then to ~0.05 MK, the characteristic temperature of AIA 304 Å channel, in another ~25 minutes. Figure 4 indicates that the temporal evolution of the disturbance speeds anti-correlates with the AIA 131 and 304 Å light curves. This means that the speed decreases during the condensation process. The smaller and larger peaks of the histogram of speeds in Figure 3(c) thus correspond to the disturbances within and without the condensation process, respectively.

The disturbances recurrently originate from the reconnection region. Along the blue dashed line in Figure 3(a), the intensity profile of the AIA 171 Å channel, spatially averaged over 3 pixels, is calculated and shown in Figure 5(a) as a black curve. We detrend the intensity profile by subtracting its smoothed intensity profile, denoted by a red curve in Figure 5(a), using a 6 minute boxcar, and display the residual intensity profile in Figure 5(b) as a blue curve. The detrended intensity profile in Figure 5(b) clearly shows the periodic variations of the intensity. We employ the wavelet-analysis technique of Torrence & Compo (1998) to retrieve the periodicity in the intensity variations. The standard “wavelet.pro” routine in the

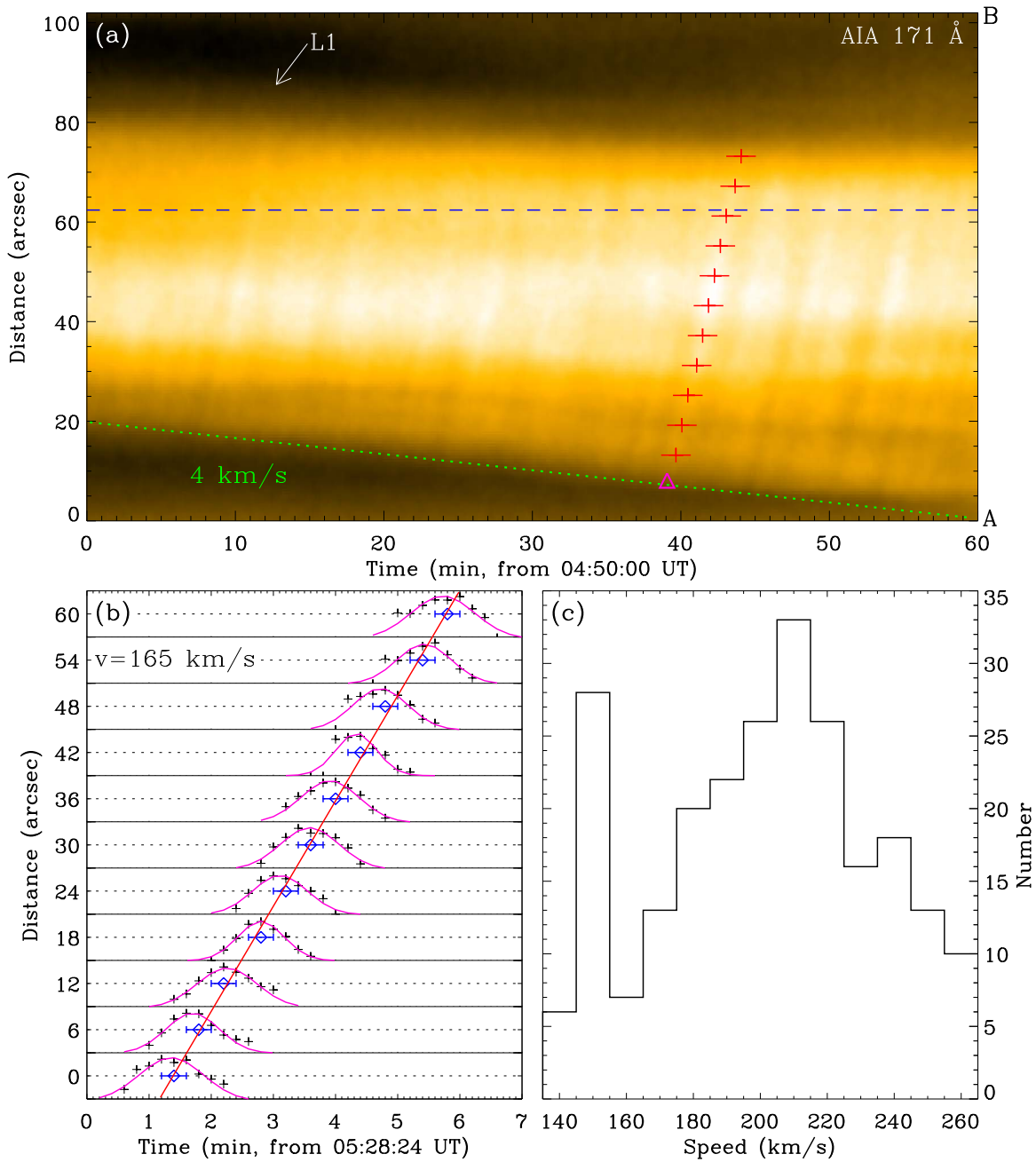


Figure 3. Measurements of the parameters of disturbances. (a) Time slice of AIA 171 Å images along the AB direction in the green rectangle in Figure 1(b). (b) Intensities (black plus symbols) of the AIA 171 Å channel at positions marked by red plus symbols along the disturbance in (a). (c) Histogram of the speeds of disturbances. In (a), the green dotted line outlines the downward motion of loops L1 at a mean speed of 4 km s^{-1} . The blue dashed line shows the position for the intensity profile of the AIA 171 Å channel displayed in Figure 5(a) by the black curve. The pink triangle marks the beginning time of the disturbance. In (b), the pink curves represent the single Gaussian profiles to the intensities. The blue diamonds and lines mark the peak positions and their error bars of the single Gaussian profiles. The red line shows the linear fit to the peak positions.

SSW package, where the “Morlet” function is chosen as the mother function, is applied to the detrended intensity profile with time cadence of 0.2 minutes and time duration of 420 minutes. The wavelet power spectrum and global wavelet power spectrum are separately displayed in Figures 5(c) and (d). Here, the confidence levels and global confidence levels are calculated employing the routine “wave_signif.pro” in the SSW package. A significant power with periods in the range of 2.5–7 minutes with a peak period at 4 minutes is evidently identified, lasting for almost 7 hr in Figure 5(c). More than 110

cycles are identified during the 7 hr, and no obvious drift of the periods is detected.

4. Summary and Discussion

Employing AIA multi-wavelength images taken on 2012 January 19, we investigated the reconnection between loops L1 and L2, as well as the coronal condensations in the MD of loops L1. During the reconnection, disturbances originating from the reconnection region are detected. They propagate upward across the MD of loops L1 with a mean speed of

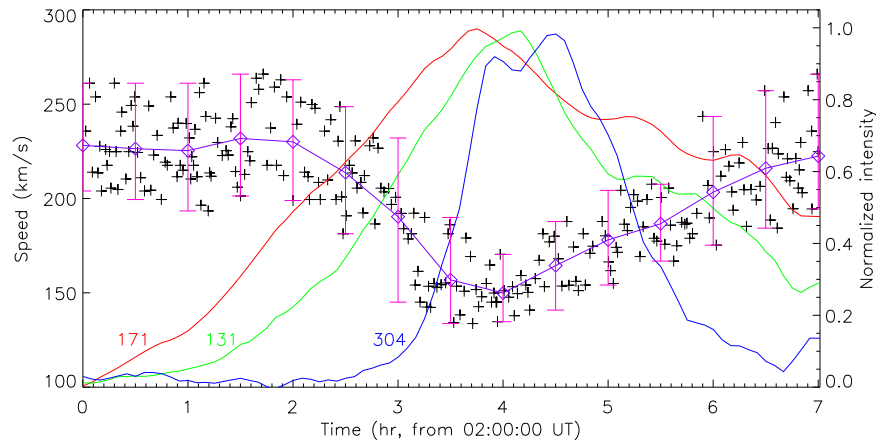


Figure 4. Temporal evolution of the speeds of disturbances. The black plus symbols show the speeds. The purple diamonds and curve indicate the mean speeds averaged in 30 minutes. The pink vertical lines denote the speed amplitudes. The red, green, and blue curves show the light curves of the AIA 171, 131, and 304 Å channels, respectively, in the green rectangles in Figures 1(b)–(d).

200 km s^{-1} in the range of $135\text{--}265 \text{ km s}^{-1}$. The speed amplitude ranges in $15\text{--}45 \text{ km s}^{-1}$ with a mean value of 30 km s^{-1} . The mean speed initially remains at a constant value of 230 km s^{-1} , then decreases to 150 km s^{-1} , and increases to 220 km s^{-1} thereafter. This temporal evolution of the mean speed anti-correlates with the light curves of the AIA 131 and 304 Å channels, which clearly show the cooling and condensation process of hotter coronal plasma in the MD of loops L1. This indicates that the speed becomes slower during the condensation process. Two peaks of the histogram of speeds with values of 150 and 210 km s^{-1} are identified, separately corresponding to the disturbances originating within and without the condensation process. The disturbances are recurrently generated, with a peak period of 4 minutes in the range of 2.5–7 minutes.

The disturbances propagate upward across the loops L1 that outline the magnetic flux in the corona. In the MD of loops L1, the Alfvén speed, v_A , is estimated using $v_A = B \times (4\pi n_p m_p)^{-0.5}$. Here B is the magnetic field strength, n_p is the proton number density, and m_p is the proton mass. The L1 loops root in the quiet Sun region, therefore B in the MD of loops L1 is small, with a value of $\sim 2 \text{ G}$ obtained from the potential field source surface (PFSS) coronal fields (Li et al. 2018). Employing n_p of $(6 \pm 0.5) \times 10^8 \text{ cm}^{-3}$ in the quiet Sun region (McIntosh et al. 2011) and B of $2 \pm 1 \text{ G}$, v_A is calculated to be $180 \pm 95 \text{ km s}^{-1}$. The sound speed, C_s , in the MD of the L1 loops is also estimated using $C_s = 152 T^{0.5}$, where C_s is in km s^{-1} , and T is the temperature in MK. As the plasma appears sequentially in AIA 171, 131, and 304 Å channels, we employ T of 0.1–0.9 MK to calculate C_s , and obtain values of $95 \pm 50 \text{ km s}^{-1}$. The speed of fast-mode magnetoacoustic waves, v_f , is $205 \pm 105 \text{ km s}^{-1}$ using $v_f = (v_A^2 + C_s^2)^{0.5}$. The observed speeds ($200 \pm 65 \text{ km s}^{-1}$) of disturbances are thus consistent with the estimated v_f . They are smaller than those previously reported (Liu et al. 2011; Shen & Liu 2012; Yuan et al. 2013; Zhang et al. 2015), caused by the slower Alfvén speed in the MD of the L1 loops with weaker magnetic field than the faster Alfvén speed in the active region loops with stronger magnetic field, but much faster than those of slow-mode magnetoacoustic waves (Zhang et al. 2015). Moreover, the disturbances are generated quasi-periodically. We thus conclude the quasi-periodic disturbances propagate across the field lines of loops with speeds consistent with those of fast-mode

magnetoacoustic waves. Hence the disturbances should represent the QFPM waves.

An increase of the wave speed following a decrease is detected. The wave speed becomes slower during the condensation process of coronal plasma, resulting in the smaller peak at 150 km s^{-1} of the speed distribution. In the MD of the L1 loops, coronal condensations lead to the increase of n_p and the decrease of T , and thus the decrease of v_A and C_s . The decrease of the Alfvén speed and sound speed in the propagating path of waves causes the decrease of the wave speeds. On the other hand, the QFPM waves may disturb the plasma in the propagating path, thereby causing the coronal condensations in the MD of the L1 loops.

Only waves propagating upward across the MD of the L1 loops, rather than other directions, are observed. This may be due to (1) the physical property, e.g., the density, magnetic field, and temperature, of the atmosphere surrounding the reconnection region as QFPM waves are trapped in regions of higher density, i.e., in regions with a slower Alfvén speed (Vršnak & Cliver 2008; Jelínek et al. 2012); or (2) the employed instrument and wavelength bandpasses (Li et al. 2016c).

The energy flux of waves, E_w , is calculated employing $E_w = 0.5 n_p m_p v_{\text{amp}}^2 v_w$. Here v_w is the wave speed, and v_{amp} is the speed amplitude. Using v_w of $200 \pm 65 \text{ km s}^{-1}$ and v_{amp} of $30 \pm 15 \text{ km s}^{-1}$, E_w is measured to be $(1.5 \pm 1.4) \times 10^5 \text{ erg cm}^{-2} \text{ s}^{-1}$, which is consistent with those previously reported (Liu et al. 2011; Shen et al. 2013). The magnetic energy flux, E_m , during the reconnection is also estimated using $E_m = (B^2 v_{in})/8\pi$. Here v_{in} is the reconnection inflowing speed. Employing the moving speeds ($5.5 \pm 3.5 \text{ km s}^{-1}$) of the L1 loops toward the reconnection region as v_{in} , E_m is calculated to be $(1.7 \pm 1.6) \times 10^5 \text{ erg cm}^{-2} \text{ s}^{-1}$, which is much smaller than those estimated during flares (Asai et al. 2004; Isobe et al. 2005). Based on these calculations, one can speculate that most of the magnetic energy may be converted to the wave energy through reconnection. This speculation is consistent with the observation that less heating and acceleration of plasma are detected during the reconnection. Moreover, different from Goddard et al. (2016) and Kolotkov et al. (2018), neither the QFPM wave radio signature nor the reconnection radio signature is detected in the Nobeyama observations. This

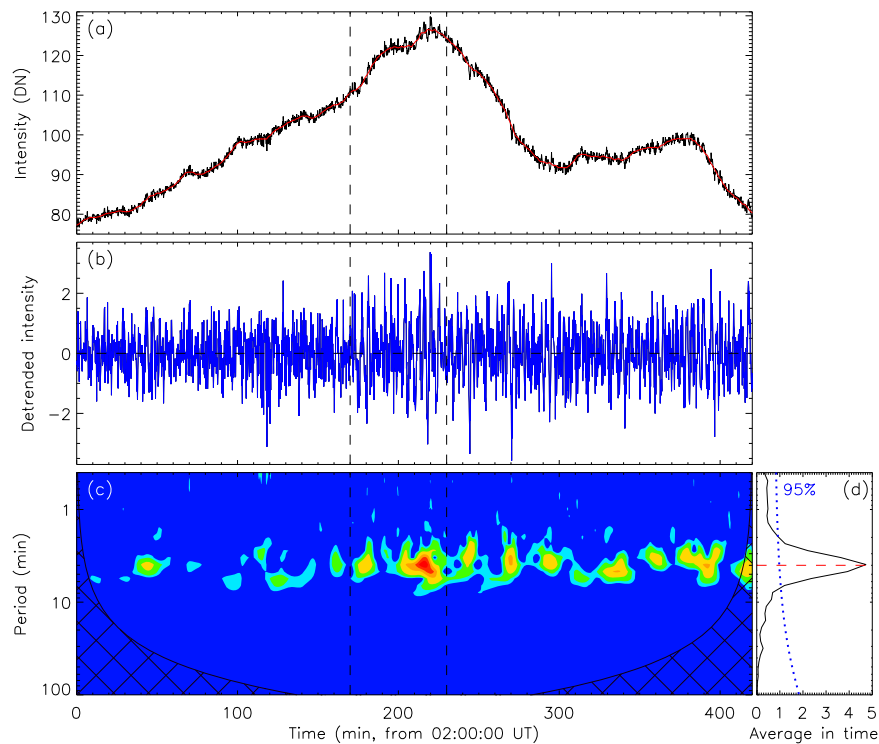


Figure 5. Wavelet analysis of the intensity profile of the AIA 171 Å channel. (a) Intensity profile (black curve) of the AIA 171 Å channel along the blue dashed line, spatially averaged over 3 pixels, in Figure 3(a), and its smoothed intensity profile (red curve) using a 6 minute boxcar. (b) Detrended intensity profile (blue curve) obtained from the intensity profile in (a) by subtracting its smoothed intensity profile. (c)–(d) Wavelet power spectrum and global wavelet power spectrum for the detrended intensity profile in (b) employing Gaussian (morlet) wavelet. The dashed vertical lines in (a)–(c) enclose the time duration of the time slice in Figure 3(a). The cross-hatched regions in (c) indicate the “core of influence” where edge affects the power. The blue dotted and red dashed lines in (d) separately mark the 95% confidence level and the 4 minute peak period.

indicates that there is no significant (detectable) nonthermal emission during the reconnection.

The waves are generated with a peak period of 4 minutes in the range of 2.5–7 minutes. These periods are consistent with the main periods of QFPM waves in Liu et al. (2011) and Kumar et al. (2017), but larger than those in Shen & Liu (2012); Yuan et al. (2013), and Nisticò et al. (2014) during flares. The QFPM waves and their associated flares are thought to originate from a common source, i.e., the reconnection releasing magnetic energy quasi-periodically during flares (Ofman et al. 2011; Shen & Liu 2012). However, no reconnection process is detected in those flares. In this Letter, no flare is observed during the reconnection. The QFPM waves directly associated with the reconnection rather than the flare are hence identified.

The QFPM waves originating from reconnection have been theoretically investigated. A steady inflow of magnetic flux, e.g., the successive downward motion of the L1 loops, toward the reconnection region could result in the repetitive and even periodic reconnection (McLaughlin et al. 2009; Murray et al. 2009). As the periodicity of waves, i.e., 4 minute peak period, is the same as that of the chromospheric oscillations, the reconnection may also be modulated by the periodic MHD oscillations (Chen & Priest 2006; Liu et al. 2011). Moreover, plasmoids and reconnection outflows produced in the current sheets during reconnection are theoretically suggested as the exciters of QFPM waves (Yang et al. 2015; Takasao & Shibata 2016; Jelínek et al. 2017). However, no plasmoid is observed here during the reconnection. More observations and theoretical studies are still needed to understand the physical

cause of QFPM waves and their general role in coronal condensations in non-flaring regions.

We thank the anonymous referee for many valuable comments that helped us to substantially improve the Letter. The authors are indebted to the *SDO* team for providing the data, and are grateful to Dr. Liping Yang for valuable discussions. The work is supported by the National Foundations of China (11673034, 11533008, 11790304, and 11773039), and Key Programs of the Chinese Academy of Sciences (QYZDJ-SSW-SLH050). L.P.C. received funding from the European Union’s Horizon 2020 Research and Innovation Programme under the Marie Skłodowska-Curie grant agreement No. 707837. This project supported by the Specialized Research Fund for Shandong Provincial Key Laboratory.

ORCID iDs

Leping Li <https://orcid.org/0000-0001-5776-056X>

Lakshmi Pradeep Chitta <https://orcid.org/0000-0002-9270-6785>

Hongqiang Song <https://orcid.org/0000-0001-5705-661X>

Chun Xia <https://orcid.org/0000-0002-7153-4304>

Yijun Hou <https://orcid.org/0000-0002-9534-1638>

References

- Asai, A., Yokoyama, T., Shimojo, M., et al. 2004, *ApJ*, 611, 557
 Aschwanden, M. 2002, *SSRv*, 101, 1
 Chen, P., & Priest, E. 2006, *SoPh*, 238, 313
 Cheng, X., Li, Y., Wan, L., et al. 2018, *ApJ*, 866, 64

- Goddard, C., Nisticò, G., Nakariakov, V., Zimovets, I., & White, S. 2016, *A&A*, 594, A96
- Huang, Z., Xia, L., Nelson, C., et al. 2018, *ApJL*, 853, L26
- Isobe, H., Takasaki, H., & Shibata, K. 2005, *ApJ*, 632, 1184
- Jelínek, P., Karlický, M., & Murawski, K. 2012, *A&A*, 546, A49
- Jelínek, P., Karlický, M., Van Doorselaere, T., & Bárta, M. 2017, *ApJ*, 847, 98
- Kolotkov, D., Nakariakov, V., & Kontar, E. 2018, *ApJ*, 861, 33
- Kumar, P., Nakariakov, V., & Cho, K. 2017, *ApJ*, 844, 149
- Lemen, J., Title, A., Akin, D., et al. 2012, *SoPh*, 275, 17
- Li, D., Ning, Z., & Su, Y. 2016a, *Ap&SS*, 361, 301
- Li, L., & Zhang, J. 2009, *ApJ*, 703, 877
- Li, L., Zhang, J., Peter, H., et al. 2016b, *NatPh*, 12, 847
- Li, L., Zhang, J., Peter, H., et al. 2018, *ApJL*, 864, L4
- Li, L., Zhang, J., Su, J., & Liu, Y. 2016c, *ApJL*, 829, L33
- Lin, J., Ko, Y., Sui, L., et al. 2005, *ApJ*, 622, 1251
- Liu, R., Lee, J., Wang, T., et al. 2010, *ApJL*, 723, L28
- Liu, W., Ofman, L., Nitta, N., et al. 2012, *ApJ*, 753, 52
- Liu, W., Title, A., Zhao, J., et al. 2011, *ApJL*, 736, L13
- Masuda, S., Kosugi, T., Hara, H., Tsuneta, S., & Ogawara, Y. 1994, *Nat*, 371, 495
- McIntosh, S., De Pontieu, B., Carlsson, M., et al. 2011, *Natur*, 475, 4177
- McKenzie, D. 2000, *SoPh*, 195, 381
- McLaughlin, J., De Moortel, I., Hood, A., & Brady, C. 2009, *A&A*, 493, 227
- Murray, M., van Driel-Gesztelyi, L., & Baker, D. 2009, *A&A*, 494, 329
- Ning, Z. 2016, *Ap&SS*, 361, 22
- Nisticò, G., Pascoe, D., & Nakariakov, V. 2014, *A&A*, 569, A12
- Ofman, L., Liu, W., Title, A., & Aschwanden, M. 2011, *ApJL*, 740, L33
- Pesnell, W., Thompson, B., & Chamberlin, P. 2012, *SoPh*, 275, 3
- Priest, E., & Forbes, T. 2000, *Magnetic Reconnection* (Cambridge: Cambridge Univ. Press), 612
- Reeves, K., McCauley, P., & Tian, H. 2015, *ApJ*, 807, 7
- Savage, S., & McKenzie, D. 2011, *ApJ*, 730, 98
- Shen, Y., & Liu, Y. 2012, *ApJ*, 753, 53
- Shen, Y., Liu, Y., Su, J., et al. 2013, *SoPh*, 288, 585
- Shibata, K. 1999, *A&SS*, 264, 129
- Su, Y., Veronig, A., Holman, G., et al. 2013, *NatPh*, 9, 489
- Takasao, S., Asai, A., Isobe, H., & Shibata, K. 2012, *ApJL*, 745, L6
- Takasao, S., & Shibata, K. 2016, *ApJ*, 823, 150
- Tian, H., Li, G., Reeves, K., et al. 2014, *ApJL*, 797, L14
- Torrence, C., & Compo, G. 1998, *BAMS*, 79, 61
- Tsuneta, S., Hara, H., Shimizu, T., et al. 1992, *PASJ*, 44, L63
- Vršnak, B., & Cliver, E. 2008, *SoPh*, 253, 215
- Xue, Z., Yan, X., Yang, L., et al. 2018, *ApJL*, 858, L4
- Yamada, M., Kulsrud, R., & Ji, H. 2010, *RvMP*, 82, 603
- Yan, X., Yang, L., Xue, Z., et al. 2018, *ApJ*, 853, 18
- Yang, L., Zhang, L., He, J., et al. 2015, *ApJ*, 800, 111
- Yokoyama, T., Akita, K., Morimoto, T., Inoue, K., & Newmark, J. 2001, *ApJL*, 546, L69
- Yuan, D., Shen, Y., Liu, Y., et al. 2013, *A&A*, 554, A144
- Zhang, Y., Zhang, J., Wang, J., & Nakariakov, V. 2015, *A&A*, 581, A78